Available online at www.sciencedirect.com

ScienceDirect

journal homepage: www.keaipublishing.com/jtte

Original Research Paper

Study of interfacial transition zones between magnesium phosphate cement and Portland cement concrete pavement

Fei Liu [a], *Baofeng Pan* [a], *Changjun Zhou* [a,*], *Ge Li* [b,**], *Xiaocun Wang* [c], *Jiaquan Li* [a]

[a] *Faculty of Infrastructure Engineering, Dalian University of Technology, Dalian 116024, China*
[b] *Tongren City Transportation Bureau, Tongren 554300, China*
[c] *Beijing Civil Aviation Design and Research Institute of China Design Group, Beijing 101318, China*

HIGHLIGHTS

- The mechanical properties of the ITZs between BFPMPC and concrete were studied for the first time.
- The ITZ-2 has roughly the same mechanical properties as the ITZ-4 between basalt aggregate and BFPMPC.
- The ITZ-3 has the worst mechanical properties among various ITZs in the repair interface.

ARTICLE INFO

Article history:
Received 16 November 2021
Received in revised form
15 June 2022
Accepted 26 June 2022
Available online 4 June 2024

Keywords:
Portland cement concrete pavement
Interfacial transition zone
Magnesium phosphate cement
Repair interface
Nanoindentation
Mechanical properties and characteristics

ABSTRACT

The Portland cement concrete pavement (PCCP) often suffers from different environmental distresses and vehicle load failure, resulting in slab corner fractures, potholes, and other diseases. Rapid repair has become one of the effective ways to open traffic rapidly. In this study, a novel type of rapid repair material, basalt fiber reinforced polymer modified magnesium phosphate cement (BFPMPC), is used to rapidly repair PCCP. Notably, the mechanical properties and characteristics of the repair interfaces which are named interfacial transition zones (ITZs) formed by BFPMPC and cement concrete are focused on as a decisive factor for the performance of the rapid repair. The changing trend of the elastic moduli was studied by nanoindentation experiments in the ITZs with the deconvolution analysis that the elastic moduli of certain kinds of substances can be determined. The experimental results show that the elastic modulus of ITZ-1 with a width of about 20 μm can be regarded as 0.098 times of the aggregate, and 0.51 times of the ordinary Portland cement (OPC) mortar. The BFPMPC-OPC mortar ITZ has roughly the same mechanical properties as the ITZ between aggregate and BFPMPC. A multi-scale representative two-dimensional model was established by random aggregate and a two-dimensional extended finite element method (XFEM) to study the mechanical properties of the repair interface. The simulation results show that the ITZ formed by the interface of BFPMPC and

* *Corresponding author.*
** *Corresponding author.*
E-mail addresses: liufei2017@mail.dlut.edu.cn (F. Liu), panbf@dlut.edu.cn (B. Pan), zhouchangjun@dlut.edu.cn (C. Zhou), 8040446@qq.com (G. Li), 44165756@qq.com (X. Wang), jiaquan123123@163.com (J. Li).
Peer review under responsibility of Periodical Offices of Chang'an University.
https://doi.org/10.1016/j.jtte.2022.06.009
2095-7564/© 2024 Periodical Offices of Chang'an University. Publishing services by Elsevier B.V. on behalf of KeAi Communications Co. Ltd. This is an open access article under the CC BY-NC-ND license (http://creativecommons.org/licenses/by-nc-nd/4.0/).

OPC mortar and basalt aggregate is the most vulnerable to failure, which is consistent with the nano-indentation experimental results.

© 2024 Periodical Offices of Chang'an University. Publishing services by Elsevier B.V. on behalf of KeAi Communications Co. Ltd. This is an open access article under the CC BY-NC-ND license (http://creativecommons.org/licenses/by-nc-nd/4.0/).

1. Introduction

As a structure of concrete pavements on the upper part of the subgrade or subbase, the Portland cement concrete pavement (PCCP) often suffers from different environmental distresses and vehicle load failure, such as slab corner cracking and potholes for PCCP. Such distress not only leads to the PCCP structure damage but also affects daily traffic. The rapid repair technology of PCCP is an effective way to relieve the inconvenience of pavement damage. The strict demandings of the rapid repair materials, such as quickly setting and fast hardening, high early strength, and satisfied durability, were possessed to solve this problem almost perfectly. Therefore, a research hotspot for the exploitation of new rapid repair materials has been deemed.

The potential materials for rapid repair of PCCP include but are not limited to sulphoaluminate cement (SC), and basic magnesium sulfate cement (BMSC), magnesium phosphate cement (MPC) (Zheng et al., 2022). The SC is suitable for filling joints and other scenes profit from the great fluidity and fast-hardening but extremely difficult to improve the fatal shortcoming of poor sustainability in the middle and late stages. Li et al. (2019) found that the compressive and flexural strength increased greatly in the middle and late periods and tended to improve its ductility and durability with 15% content of the gypsum. Additionally, nanomaterials such as graphene oxide (GO) were added to SC with different degrees of growth at different ages (Liu et al., 2020). However, the increase of compressive strength and flexural strength at 24 h age was only 5.8% and 1.4%, respectively, compared with that without graphene. In a nutshell, both the improvement of hydration products and auxiliary nanomaterials can improve the shortcomings of SC effectively. Whereas, a lack of continuity for strengths in the middle and late stages still exists. BMSC, a new type of magnesium cementing material with admixture technology, is mainly composed of light-burning magnesium oxide, magnesium sulfate with different crystal water, mineral admixtures, and chemical admixtures. Although through the unremitting efforts of scholars (Wang et al., 2018; Wu et al., 2015), the strength, water resistance, and cohesiveness of BMSC have been greatly improved, the high price of raw materials is the main factor for limited development (Xu et al., 2020). The current research is limited to the development of novel mixing technology (Zeng and Yu, 2020) to expect the improvement of its basic mechanical properties (Tan et al., 2020). In addition, it is easy to crack due to the excessive thermal stress of cement pastes caused by high temperatures.

MPC, a mixture of dead burnt magnesium oxide, a soluble phosphate, borax retarder, and water in a certain proportion, is mainly generated by the acid-base neutralization reaction between soluble phosphate and magnesia to produce an inorganic cementing binding material. Due to the high crystallinity of its products, it is called phosphate chemistry-ceramic bonded materials. With its high early strength, well durability, thermal stability, and water resistance, it has become the subject of this research. In recent years, there have been many reports on MPC (Yang et al., 2014), mainly focusing on the improvement of mechanical properties (Feng et al., 2016), durability (Le Rouzic et al., 2017), and in-depth research on the effects of hydration products (Qin et al., 2021). The incorporation of an appropriate amount of polymer reduces the brittleness of the concrete while increasing flexibility and deformability. The internal pores of the matrix filled by the polymer form a three-dimensional spatial network structure (Zhou et al., 2020), significantly improving the abrasion resistance of concrete materials and facilitating road repair. The mechanical properties and durability of concrete are improved by the addition of fiber. Feng et al. (2021) added 1.2%–2.0% (volume fraction) of polyvinyl alcohol (PVA) fiber and found that the workability of the developed fiber-reinforced MPC-based composites decreases slightly with the increase of fiber volume fraction and the superior bond behavior between the PVA fibers and MPC matrix. Qin et al. (2018a) showed that MPC material toughened by basalt fiber has an application advantage over glass fiber in performance.

Cement concrete is composed of aggregate, cement mortar, and interfacial transition zone (ITZ) (Dong et al., 2023; Gao et al., 2019; Zhu et al., 2017). Among them, the ITZ, as the weakest portion in the structure, often fails firstly, weakening the performance of the concrete structure. Therefore, some researches on ITZ have been carried out by domestic and foreign scholars, including experimental testing and numerical model development. Nanoindentation technology (Königsberger et al., 2018) and atomic force microscope (AFM) (Gao et al., 2019) have been widely used in recent years to measure the microstructure of ITZ. Golewski (2021) studied the contribution of fly ash to ITZ, and the results showed that the addition of fly ash had a positive effect on the reduction of the interface microcrack size of concrete composites under dynamic load, and the effect was the best when the FA dosage was 20%. Kim and Abu Al-Rub (2011) developed a mesoscale calculation model for the plastic damage response of ITZ cement-based composites. They believed that the polygonal aggregate model had stress concentration at sharp edges, and its ultimate tensile strength and damage initial strain was closer to reality, which also directly proved the inapplicability of the circular aggregate model. Also, the ultimate tensile strength of concrete increases linearly with the increase of ITZ strength. Faced with many experimental results of interface fracture

and fracture energy data, an artificial neural network (ANN) was used to train and verify the data pool, and the real ITZ tensile strength and fracture energy were obtained, which is an excellent research trend. Xi et al. (2021) used ANN to predict the fracture characteristics of ITZ in concrete at the mesoscale. The results show that the fracture model can reproduce the cracking phenomena of concrete at a mesoscale (such as micro-crack initiation, crack deflection, crack bridge, etc.). However, the disadvantage that needs to be solved is that the data of interface fracture cannot be directly applied to the 3D mesoscale fracture simulation of concrete by using ANN. It is necessary to optimize the fracture performance of ITZ by minimizing the objective function established by ANN with good results.

When the traffic loads are applied to the repair area, whether MPC can be used as a sustainable repair material is determined by the shear resistance, durability, and mechanical properties of the repair interface. However, rare reports (Liu et al., 2022) on the mechanical properties and characteristics of the repair interface between PCCP and MPC. The properties of the interface should be explored to explain the mechanism of the repair interface.

In the previous research (Liu et al., 2021), the shear properties of the composite specimens of MPC as a repair material and OPC paste were investigated, and the interface constitutive model was studied. Although the interface damage model of MPC and PCP was achieved, the other types of bonding were not considered in detail, including the interface between MPC and aggregate, between MPC, and the interface of aggregate and Portland cement.

Consequently, a novel basalt fiber-reinforced polymer-modified magnesium phosphate cement (BFPMPC) was used for rapid repair to form the complex repair interface between BFPMPC and PCCP in service as the objective. Firstly, the mechanical properties of this interface are investigated, and the elastic modulus near the ITZ was obtained initially by the nanoindentation experiment. Secondly, the variation trend of mechanical properties in the ITZ was analyzed by the deconvolution method statistically. Thirdly, a finite element model was established by generating random aggregate and two-dimensional extended finite element method (XFEM) to simulate and predict the weakest position of the ITZ. In the end, the difference and relationship of elastic modulus of each ITZ based on the above research will lay a foundation for further study of constitutive relationship and mechanical analysis of ITZ.

2. Raw materials and methodology

2.1. Raw materials

In cement concrete, the aggregate is basalt. The P.O. 42.5R high-early-strength ordinary Portland cement (OPC) produced in Dalian was chosen. The water-cement ratio of PCC is 0.44 and the cement content is 445 kg/m^3. In BFPMPC, dead burnt magnesia from Xinhemei Factory in Haicheng City, was selected. Fly ash with Grade II produced by power plant in Gongyi was used. The type of ECO 7623 butadiene-styrene copolymer emulsion produced by BASF in Germany was used. Basalt fiber with a length of 12 mm and a diameter of 17.4 μm was produced by Shanghai Chenqi Chemical Technology Co., Ltd. The water-cement ratio of BFPMPC is 0.18, and the mass ratio between dead burnt MgO and phosphate is 2.5:1. The mix proportion of BFPMPC and cement concrete are shown in Tables 1 and 2. Specimens are composed of BFPMPC at 6 h and 3 d curing ages and old Portland cement concrete (PCC) which are named Sample-6h and Sample-3d, respectively.

2.2. Methodology

Due to distress including slab corner cracking, and potholes happened, the aggregate surface in concrete may be exposed. Therefore, the repair at the joint will form various interfacial interfaces between MPC and concrete (Qin et al., 2018b) (Fig. 1). The ITZ between aggregate and OPC mortar in the PCC was named ITZ-1. Then, the ITZ formed between MPC mortar and ordinary Portland cement (OPC) mortar, the MPC mortar and ITZ-1, and the MPC mortar and the exposed aggregates were named ITZ-2, ITZ-3, and ITZ-4, respectively.

To study the mechanical response of the ITZ as shown in Fig. 1, a finite element model was established and simulated by ABAQUS software. Firstly, the cement concrete model was established. The random aggregate generation code is written in Python and inserted into ABAQUS to generate representative elements. Secondly, the various ITZs in the schematic above in the ITZ were defined, in the study, considering the ITZ of mortar and aggregate in cement concrete, ITZ-1 was generated at the same time as random aggregate, as shown in Fig. 2. The size, element number, and element type of the model are shown in Table 3. Based on the previous interface damage constitutive relationship between BFPMPC and cement concrete (Liu et al., 2021), as shown in Fig. 3, damage constitutive is defined at the repair interface, as shown in Eqs. (1) and (2).

$$\tau(u)=\begin{cases} D_0Gu & u\le u_0 \text{ (perfectly bonded)} \\ \tau_0+D_1G(u-u_0) & u_0<u\le u_1 \text{ (partial debonded)} \\ \tau_{\max}-D_2G(u-u_1) & u_1<u\le u_2 \text{ (fully debonded)} \\ [\tau_{\max}-D_2G(u_2-u_1)]e^{(u-u_2)/u_2} & u_2<u \text{ (frictional sliding)} \end{cases} \tag{1}$$

$$D=1-\omega=1-\frac{dA_d}{dA} \quad u\le u_0, u_0<u\le u_1, u_1<u\le u_2 \tag{2}$$

Table 1 – Mix proportion of BFPMPC (kg/m^3).

Project	Potassium dihydrogen phosphate	Dead burnt magnesia	Water	Borax	Fly ash	Basalt fiber	ECO 7623
BFPMPC	185.2	462.8	129.6	46.3	72	3.3	43.2

Table 2 – Mix proportion of cement concrete (kg/m^3).

Water	Cement	Aggregate	Sand	Water reducing agent	Air entraining agent
168	420	1235.5	636.5	3.78	0.042

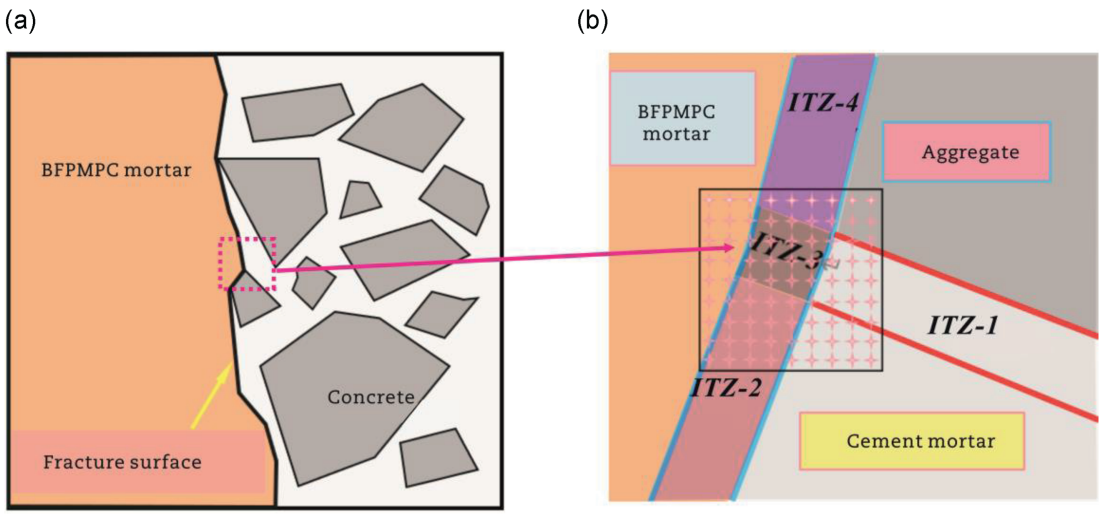

Fig. 1 – Theoretical analysis diagram for ITZs. (a) Rapid repair for cement concrete. (b) Analysis and nanoindentation tests for ITZs.

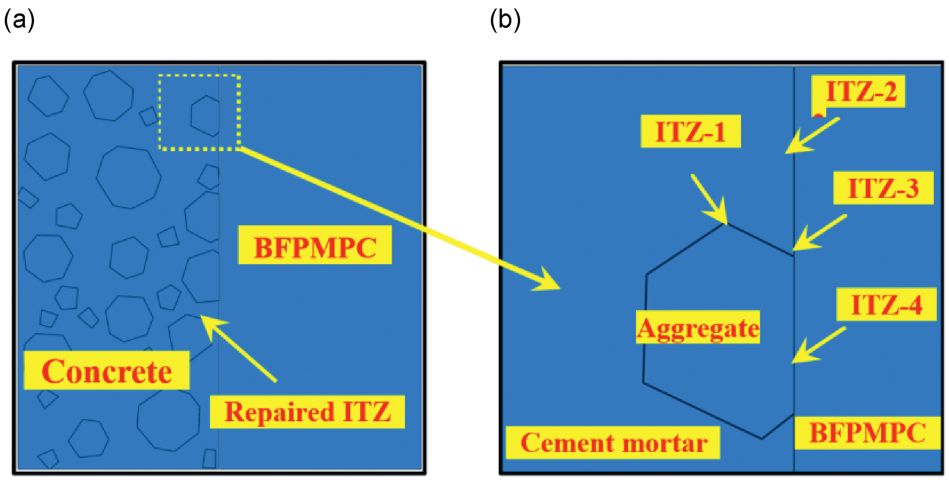

Fig. 2 – Two-dimensional model of ITZ. (a) Interface model for numerical simulation. (b) Enlarged zone for sub-ITZ in the repair interface.

Table 3 – Size, element number, and element type of the model.

Project	Size	Element type	Element number
Cement concrete	200 mm × 100 mm	CPS4R	5402
BFPMPC	200 mm × 100 mm	CPS4R	800
ITZ	20 μm × 200 mm	CPS3	512

where the τ is the interfacial shear strength, u is the displacement of MPC or BFPMPC mortar relative to cement concrete, u_0 is the ultimate displacement at the perfect bonded stage, u_1 is the displacement corresponding to peak damage force for the partial debonded stage, u_2 is the displacement for the fully debonded stage, G is the shear moduli, which is calculated from the elastic modulus for the nano-indentation test, τ_{max} is the maximum interfacial shear strength of ITZ for failure, D is the damage factor, ω is a ratio, dA_d is the acreage of the fraction debonding of the ITZ, dA is the whole bonding area of the interface.

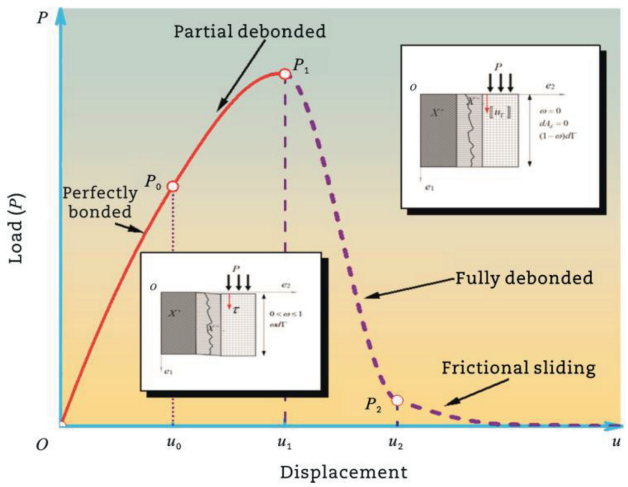

Fig. 3 – Interface damage model (Liu et al., 2021).

2.3. *Nano-indentation test*

Since the mechanical properties of the ITZ between MPC and PCC were rarely studied, the mechanical parameters for numerical simulation with shear and tensile states were obtained from experimental tests. For the circumscribed size and mechanical properties and characteristics of the ITZ, the grid nanoindentation was used to study the mechanical properties to obtain its elastic modulus.

The nanoindentation technology is tested by the Hertz contact theory and creep model to press the test head into a plane to obtain the continuously load-displacement curve, indentation moduli, elastic, plastic, and fracture energy, as shown in Fig. 4.

The nano-indentation instrument is named HYSITRON® Triboindenter TI 980 with the imaging technique for information on the surface of sample real-time used. The standard BERKOVICH probe with a 65° semi-vertical angle and 150 nm curvature radius is chosen as a test probe in the grid nanoindentation test. As the Berkovich indenter, the elastic parameter is the elastic modulus of 1141 GPa and Poisson's ratio of 0.07. The quartz sample needs to be tested to calibrate the test platform before starting the test. The elastic properties of ITZ were focused on in this study by this loading method. Furthermore, the indenter load P and the indenter depth h were measured. The typical P-h curve with increasing loading, is followed by a short holding and decreasing unloading, as can be seen in Fig. 4. A standard trapezoidal loading history should be set as three parts: loading, holding, and unloading which is prescribed in ISO 14577 and ASTM 2808. The researchers used different loading times to study material properties. For example, Suwanmaneechot et al. (2020) kept loading for beyond 300 s to explore the creep behavior of C-S-H under different drying relative humidities. da Silva et al. (2014) and Karimzadeh et al. (2019) used about 10 s holding time to study the ultra-high performance cementitious composites. Zhang et al. (2018) also tested 2 s for holding time to study the soil and stone material. Generally, the inorganic nonmetallic material needs a longer loading holding time for dwelling. The loading of nano-indentation is defined by $T_{\text{loading}} = 10$ s for loading time, the dwelling for holding time $T_{\text{holding}} = 5$ s at $P_m = 3000\,\mu$N, and unloading time $T_{\text{unloading}} = 10$ s and a displacement from 0 to 10 μm. Then, by the Hertz contact theory, the elastic modulus and hardness of ITZ were calculated by Eqs. (3)–(5).

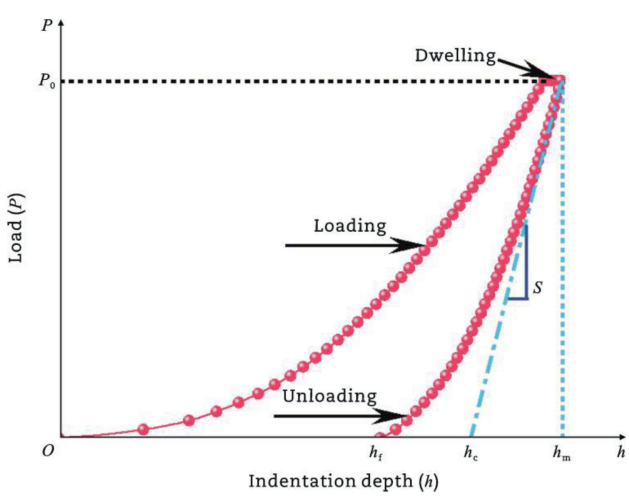

Fig. 4 – Schematic of nanoindentation test.

$$E = \frac{S}{2\sqrt{A}}\sqrt{\pi} = \frac{dP/dh}{2\sqrt{A}}\sqrt{\pi} \tag{3}$$

$$\frac{1}{E} = \frac{1-\mu_1^2}{E_1} + \frac{1-\mu_2^2}{E_2} \tag{4}$$

$$H = \frac{P_0}{A} \tag{5}$$

where P_0 is the peak value of force for the indenter in the grid nanoindentation experiment, the elastic modulus of the sample is related to the measured reduced modulus E, E_1 is the elastic moduli for the indenter, and μ_1 is the Poisson's ratio for the indenter, the E_2 and μ_2 are the elastic moduli and Poisson's ratio of the ITZs, H is the hardness of the each point for ITZ, S is the slope of the unloading curve in Fig. 4.

The specimens are made with the following steps. First, the old cement concrete test block was grinded to a block (20 mm × 20 mm × 10 mm). Then, it was placed in the steel mold, and mixed by BFPMPC mortar into the mold to a block with 20 mm × 20 mm × 10 mm. After 30 min, the mold is removed and placed in the air-cured after 6 h and 3 d. Until reaching the curing ages, the sides are sanded and polished. The production process is completed, and the specimens are immersed in ethanol for 24 h to terminate hydration.

3. Results and discussion

3.1. *Nanoindentation test*

According to the position selected by the microscope on the nanoindentation test, the ITZ of Sample-6h and Sample-3d were tested by the nano-indentation with dot matrix. The dot-matrix is 10 × 14 = 140 points, which included 10 test lines and marked as lines 1 to 10, and so on. Notable each point is 5 μm apart, and each line is 10 μm apart. After the nano-indentation test was conducted, the elastic moduli were calculated by Eqs. (3)–(5) with different positions for grid nanoindentation as shown in Fig. 5. The elastic moduli of cement mortar, aggregates, and basalt fiber are about 13.4 GPa, 74.5 GPa, and 85–115 GPa, respectively (Sun et al., 2019), which can be used as a reference to determine the boundary for OPC mortar and aggregate from Fig. 5.

Firstly, the elastic modulus variation of ITZs in the samples was analyzed by the statistical results for Fig. 5, as shown in Table 4. The elastic moduli of the ITZ of cement mortar and aggregate are 8.46 GPa and 8.71 GPa respectively for 6 h and 3 d with similar values and little error. The elastic moduli of the basalt aggregate in the 6 h and 3 d samples is 86.05 GPa and 88.35 GPa for 6 h and 3 d by measurement, respectively. For Sample-6h, the elastic modulus of ITZ-1 is 9.83% of the aggregate, and 9.86% for 3 d. Therefore, the elastic modulus of ITZ-1 can be regarded as 0.098 of the aggregate. The data will be used for further research in the future.

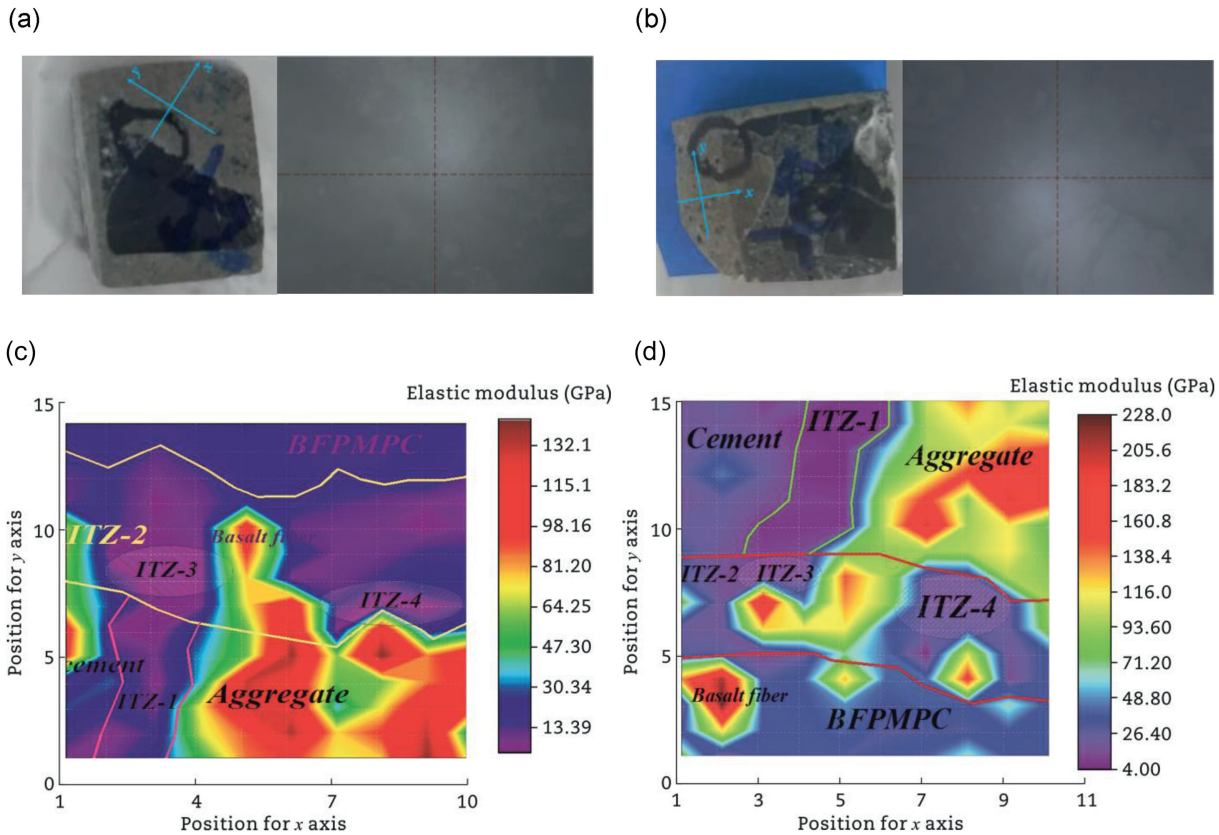

Fig. 5 – Nanoindentation test results. (a) Optical microscope diagram for Sample-6h. (b) Optical microscope diagram for Sample-3d. (c) Nanoindentation test results for Sample-6h. (d) Nanoindentation test results for Sample-3d.

Table 4 – Results from the deconvolution analysis with reference values from literature and the values from experiments.

Microstructure		Elastic modulus (GPa)		
		Reference	Nanoindentation test	Deconvolution analysis
Micro porosity		9.1 ± 2.3 (Constantinides, 2002)	–	4.46 ± 2.67 (6 h) 6.30 ± 1.09 (3 d)
Sand		73.0 ± 1.6 (Acker, 2001)	–	72.15 68.95
Aggregate		100.8 (Piasta et al., 2017)	86.05 (6 h) 88.35 (3 d)	85.56 ± 0.30 97.87 ± 0.36
Basalt fiber		85.0 (Sun et al., 2019)	104.10 (6 h) 114.50 (3 d)	94.54 ± 22.40 106.44 ± 2.41
LD C-S-H		20.2 ± 2.0 (Acker, 2001)	–	16.98 ± 0.08 (6 h) 22.70 ± 0.70 (3 d)
HD C-S-H		32.3 ± 2.6 (Mondal et al., 2007)	–	30.62 (6 h) 30.11 ± 0.28 (3 d)
ITZ	ITZ-1	–	8.89 ± 0.07 (6 h) 10.95 ± 1.60 (3 d)	8.46 (6 h) 8.71 (3 d)
	ITZ-2		12.14 ± 0.78 (6 h) 16.07 (3 d)	12.89 (6 h) 20.71 (3 d)
	ITZ-3		6.48 ± 0.13 (6 h) 13.14 ± 0.27 (3 d)	6.81 (6 h) 14.58 (3 d)
	ITZ-4		10.85 (6 h) 24.39 ± 0.31 (3 d)	11.19 (6 h) 22.89 (3 d)
	ITZ		14.91 ± 0.04 (6 h) 21.55 (3 d)	11.01 (6 h) 21.14 (3 d)
BFPMPC		37.3 (28 d) (Li et al., 2018)	18.18 (6 h) 35.92 (3 d)	18.42 (6 h) 39.68 ± 0.29 (3 d)
FA		32.4 ± 5.1 (Das et al., 2015)	–	37.01 (6 h) 34.20 ± 0.26 (3 d)
Cement mortar		20.8 (Yang, 2003)	19.20 (6 h) 21.32 (3 d)	19.50 ± 0.04 19.15 ± 0.20

For the ITZ formed by BFPMPC mortar bonding old cement concrete, ITZ-2, ITZ-3, and ITZ-4 will appear as shown in Fig. 5(c) with the elastic modulus of the ITZ is analyzed respectively. For ITZ-2, the elastic modulus gradually increases with the growth of age, which is consistent with previous research results (Liu et al., 2021). The elastic modulus of ITZ-4 formed by BFPMPC mortar and aggregate also increases with age, both 6 h and 3 d are larger than the elastic modulus of the entire ITZ, which is close to the elastic modulus of ITZ-2. Therefore, when BFPMPC mortar repairs cement concrete, the elastic moduli are shown in the region of ITZ-2 or ITZ-4 without the characteristics of weak mechanical properties. It shows that the elastic modulus of ITZ-3 is gradually increasing with the age, which is still the region with the smallest elastic modulus compared with ITZ-2 and ITZ-4. For the above analysis, ITZ-3 caused by the ITZ-1 between OPC mortar and aggregate is the area with the weakest mechanical properties in the entire repair interface. Therefore, the influence of width and mechanical properties of ITZ-1 and ITZ-3 on the repair properties of BFPMPC mortar should be emphasized.

3.2. *Deconvolution calculation and analysis*

Generally, the elastic modulus of hydration product for cement material accords with Gaussian distribution. OPC is a heterogeneous material containing many inclusions. Multiple grid nanoindentation tests and scientific statistical analysis are required for nano-indentation experiments. It is often necessary to remove an outlier in the test area. In a statistical sense, every nanoindentation data is actually regarded as a single statistical event, so the data features extracted from the analysis of continuous indentation measurements are used as random variables. For example, 100 indentations are sufficient to ensure that the elastic properties of LD and HD C-S-H converge with a deviation of less than 5% (Sorelli et al., 2008). In this study, not too many data points need to be selected, on account of the cement paste without particularly large particles.

The data are analyzed by the discrete experimental distribution values $D(\chi)$ of the mechanical property $\chi = (M, H)$ is deconvoluted into the sum of n theoretical probability distribution functions D_j (one for each machine with different phases).

$$\min D(\chi) = \sum_{i=1}^{N} \sum_{\chi=(M,H)} \left[\sum_{j=1}^{n} f_j D\left(\chi_i, \mu_j^{\chi}, \delta_j^{\chi}\right) - D(\chi_i) \right]^2 \tag{6}$$

where N is the number of intervals (bins) by which the problem is discretized, f_j is the volume fraction of the phase composing the heterogeneous material, μ_j^{χ} and δ_j^{χ} are the mean and standard deviation of $\chi = (M, H)$ with the phase $j = 1, 2, \cdots, n$, $D(\chi_i)$ is the theory probability density distribution of N nano-indentation test points.

$$D(\chi_i) = \frac{i}{N} - \frac{1}{2N} \qquad i \subseteq [1, N] \tag{7}$$

For the multi-variable distribution model, the least variance method can be used to deconvolution the mixed Gaussian function. The algorithm based on linear minimum variance criterion is optimal. The nano-indentation values were solved by minimizing the square deviation method. The frequency density diagrams of the elastic modulus at 6 h and 3 d were shown in Figs. 6 and 7, respectively. The deconvolution calculation of the experimental probability distribution function (PDF) and the best-estimated PDF of each microstructure were also shown in Figs. 6 and 7. The simulated PDF is the sum of single-phase PDF evaluated from the deconvolution analysis for the elastic modulus.

The results in Figs. 6 and 7 are compared with the experimental data of the direct nano-indentation analysis method in Table 4. The error between the two analysis methods is also small, indicating that the deconvolution analysis method is scientific to some extent. Secondly, for example, the elastic modulus of inclusions such as HD C-S-H, LD C-S-H, the void, sand, and FA in cement mortar can not be obtained by direct analysis of nano-indentation experimental data. It reflects the necessity of the deconvolution method in the analysis of nanoindentation experimental data.

3.3. *Relationship among ITZs*

The theoretical schematic diagram in Fig. 1 was formed that the ITZ is generated when BFPMPC mortar is repairing cement concrete. Due to the complex particularity of the contact surface, it is divided into several ITZ components. In concrete, OPC mortar, aggregate, and the ITZ formed by OPC mortar and aggregate have an influence on the repairing interface. In addition, according to the deconvolution analysis and nanoindentation experimental data, ITZ-3, as the area where the repair interface and ITZ-1 with combined action, have the weakest mechanical properties. Therefore, it is necessary to conduct an in-depth discussion on the relationship with the ITZs.

The elastic modulus of ITZ-1 with a width of about 20 μm can be regarded as 9.8% of the aggregate and 0.51 of the OPC mortar, according to the value in Table 4 and Figs. 6 and 7. The situation of each ITZ is shown in Fig. 8.

Compared with the Sample-6h, the elastic moduli of ITZ-3 and ITZ-4 for 3 d increased to 102.7% and 124.8%, respectively. Different contact materials have different effects on the growth of elastic modulus. Perhaps for its good chemical compatibility, a stable interface structure is formed by BFPMPC and OPC mortar at 6 h. Therefore, with the growth of age, the elastic modulus of ITZ-2 increases slightly. As for the aggregate, the basalt material is relatively single and the crystal arrangement is relatively homogeneous, the elastic modulus of ITZ-4 is greatly affected by the mechanical properties of BFPMPC hydration products. For ITZ-1, whose mechanical properties are extremely unstable, when effective mechanical bonding and chemical compatibility have not been formed at 6 h, the mechanical properties of ITZ-3 are the weakest, which may be the most direct factor of early structural failure. When the age reaches 3 d, the elastic modulus increases greatly. However, it is still the weakest area in the mechanical properties of the repair interface.

Additionally, two forms of ITZs are related to the basalt fiber in BFPMPC. One is the basalt fiber in BFPMPC paste, the other is the basalt fiber in the ITZ formed by BFPMPC and cement concrete, as can be seen in Fig. 9. The elastic moduli of

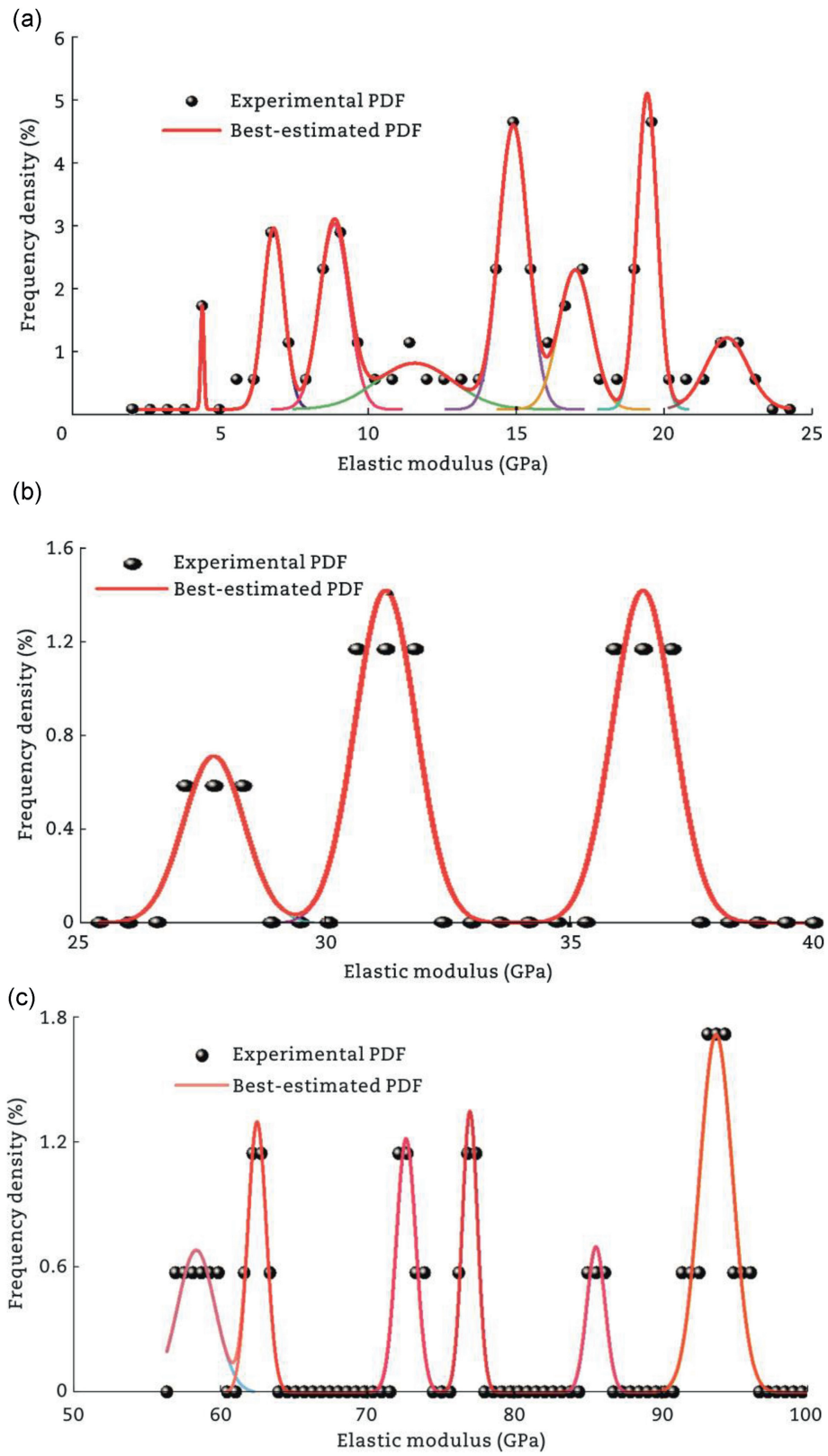

Fig. 6 – Frequency density diagrams of the elastic modulus at 6 h. (a) Elastic modulus from 0 to 25 GPa. (b) Elastic modulus from 25 to 40 GPa. (c) Elastic modulus from 50 to 100 GPa.

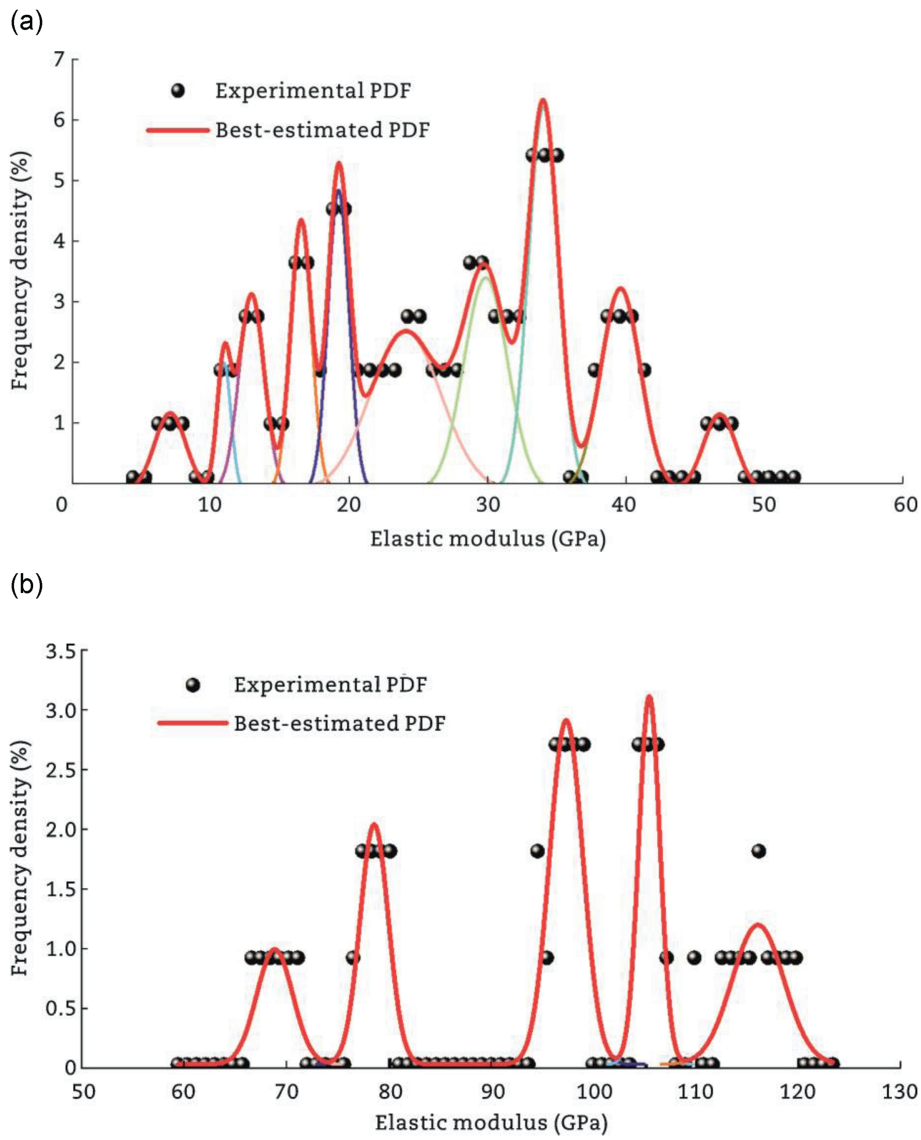

Fig. 7 – Frequency density diagrams of the elastic modulus at 3 d. (a) Elastic modulus from 0 to 55 GPa. (b) Elastic modulus from 55 to 130 GPa.

these two ITZs are different. Some conclusions were obtained from the nano-indentation data and deconvolution analysis results as follows. For the ITZ on basalt fiber in the repair interface in Sample-6h, the average elastic modulus of ITZ within the 10 μm range of basalt fiber is 17.06 GPa, and that outside 10 μm of basalt fiber is 8.48 GPa, which is due to the low elastic modulus of the main matrix phase in the repair interface. In the BFPMPC paste, the average elastic modulus of ITZ is 62.01 GPa in the range of 10 μm close to the basalt fiber, and 58.37 GPa in the part beyond 10 μm. The difference in elastic modulus for ITZ is small and shows a downward trend. According to the development status of elastic modulus, it should be consistent with the BFPMPC at the distance from the fiber.

For the repair interface in Sample-3d, the average elastic modulus is 30.21 GPa in the distance of 10 μm from the basalt fiber, and 22.09 GPa in the area over 10 μm. In the BFPMPC paste, the average elastic modulus of the basalt fiber within 10 μm is 78.93 GPa, and the average elastic modulus of the basalt fiber over 10 μm is 31.39 GPa. It also indicates that age has a great influence on the elastic modulus of ITZ around basalt fibers.

3.4. *Numerical simulation on ITZs*

3.4.1. *Model development*

In this paper, two-dimensional modeling was adopted to establish representative elements for finite element analysis (FEA). Random aggregates, as well as ITZ-1, were generated. An example of numerical simulation is 3 d curing age. As can be seen from Fig. 2, cement concrete is on the left and BFPMPC repair material is on the right. The ITZ (repair interface) is set in the middle, and the corresponding ITZ-2, ITZ-3, and ITZ-4 are set on the repair interface. Additionally, the thickness of each ITZ was measured by Figs. 6 and 7, as well as the data from deconvolution analysis were required for setting ABAQUS parameters, as shown in Table 5. Notably, the overall dimensions of the ITZ are 20 μm × 200 mm with 512

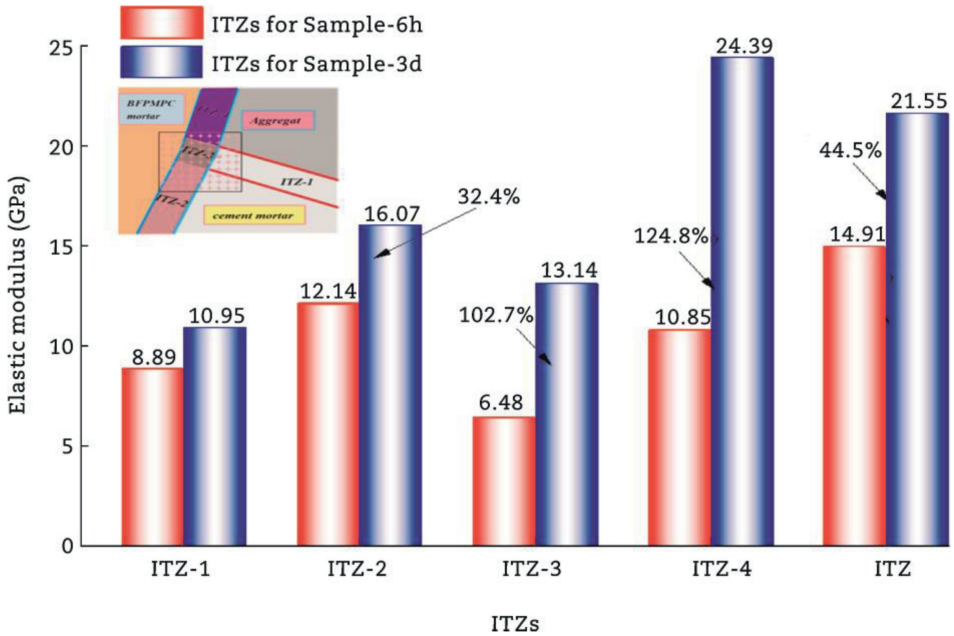

Fig. 8 – Elastic modulus for ITZs.

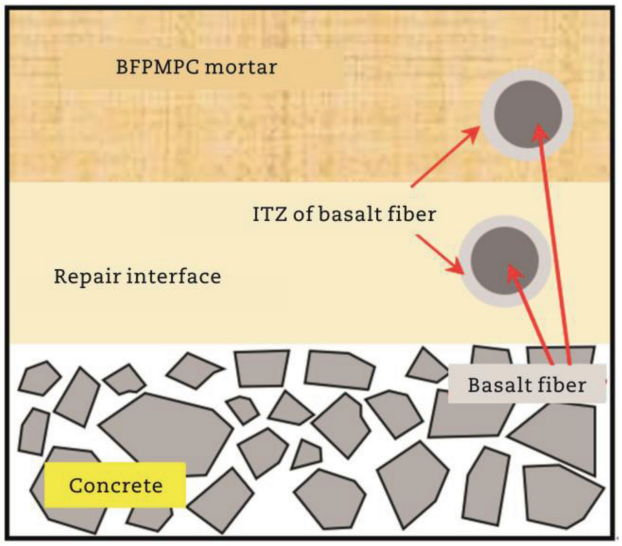

Fig. 9 – Schematic diagram of ITZ for basalt fiber.

Table 5 – The parameters for simulation in ITZs at 3 d curing ages.

Project	Curing age (d)	Elastic modulus (GPa)	Poisson's ratio	Thickness (μm)
ITZ-1	3	10.95	0.20	15
ITZ-2	3	16.07	0.25	20
ITZ-3	3	13.14	0.20	20
ITZ-4	3	24.39	0.20	20
BFPMPC	3	39.68 ± 0.29	0.25	–
Concrete	–	23.76	0.22	–
Cement mortar	–	13.40	0.25	–
Aggregate	–	74.50	0.15	–

elements total. For ITZ-2, its overall size depends on the contact length between the repair interface and ordinary Portland cement mortar. For ITZ-3, it depends on the width of ITZ-1. For ITZ-4, it depends on the contact length between the repair interface and the coarse aggregate.

The interface was fractured by the action of 10 kN traction force for shear states which were applied to the BFPMPC side, studying the force and stress distribution of various interfaces in the repair interface. This data is from the shear strength data in the previous study (Liu et al., 2022), in which the pure shear test was used to evaluate the bonding strength of BFPMPC to cement concrete, and its failure peak value was about 10 kN. The boundary conditions are set as the cement concrete fixed and the BFPMPC without constraint. As shown in Fig. 10(a) with the details of the boundary condition setting, to match the field condition of concrete pavement repair, the fixed constraint boundary condition is adopted for cement concrete with a shear failure, and an unconstrained boundary condition is adopted for repairing material BFPMPC. The displacement loading method is used in the simulation and the loading rate is 0.5 mm/min, which is the same as the shear experiment in the previous study. However, the function of simulation for the tensile test is to observe the interface force under the force of 10 kN without corresponding experimental data, and the loading rate is 0.5 mm/min.

3.4.2. *Shear fracture*

The mechanical response of the repair interface with a shear state was simulated, as the second case for numerical simulation. The failure, in this case, is like a bond-slipping with the shear failure at the interface. In general, the situation of failure is divided into four steps at the interface. First, the interface is perfect bonding, and the damage led to performance degradation in partial debonding at the second step with the continuous loading. As the

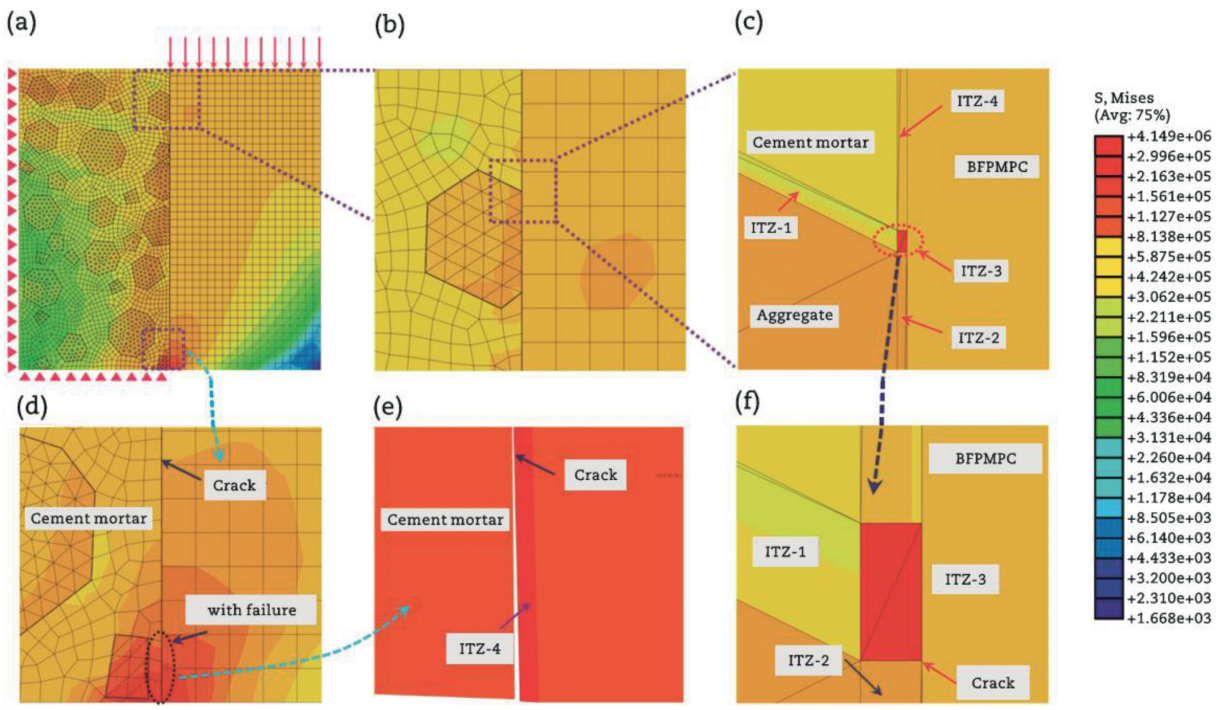

Fig. 10 – Failure of repair interface in a shear state. (a) Mises nephogram of repair interface shear damage. (b) Partial enlargement nephogram for interface shear damage. (c) Mises nephogram of ITZ-3. (d) Damage fracture of repair interface edge position. (e) Detail of damage fracture for edge position of repair interface. (f) Enlarged view of damage fracture in the ITZ-3 region.

ultimate bonding strength is reached, the interface begins to break with the obvious stiffness degradation in perfect debonded. In the end, the frictional sliding part loses its stiffness at last.

As shown in Fig. 10, the mechanical response is more intense in the upper part of the interface. The stress state near ITZ-3 was almost consistent with that of the repair interface under the tensile state in Fig. 12. Notably, the trend of fracture in the shear state is different from that in the tensile state, as can be seen in Fig. 10(d)–(f). In the shear state, cracks developed from the upper end of the interface to the vicinity of the ITZ-3 area while in the tensile state (Fig. 12), cracks developed from the middle of the repair interface. It also inferred that when BFPMPC is used as a repair material for cement concrete pavement, more attention should be paid to the shear strength. It is not difficult to explain that the interface is subjected to shear force, and the bearing limit is exceeded with the bonding strength on the repair interface, resulting in fracture failure. In particular, the crack was prone to developing from the upper part of the weakest ITZ, i.e., ITZ-3 from the perspective of mechanics.

In terms of verification of model calculation results, 3 d shear strength 3.98 MPa of BFPMPC-concrete was obtained by formula calculation in the previous paper, and the numerical simulation result was 4.15 MPa, with an error of 4.3%. On the one hand, the reliability of the constitutive relationship in the shear model is demonstrated, as can be seen in Fig. 11.

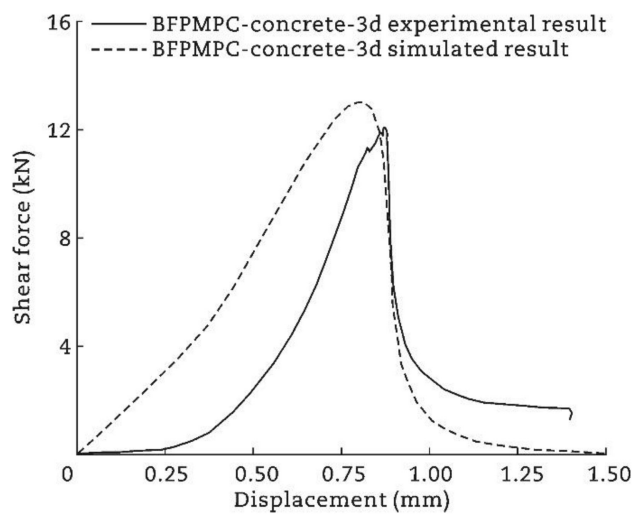

Fig. 11 – Load-displacement curve for the shear strength.

Secondly, the shear strength and shear state are consistent with the experimental results.

3.4.3. *Tensile fracture*

Tensile fracture on ITZs was simulated in this section and the corresponding numerical results are shown in Fig. 12. When BFPMPC is subjected to axial tension, both ends of the repair interface showed an obvious mechanical response to the

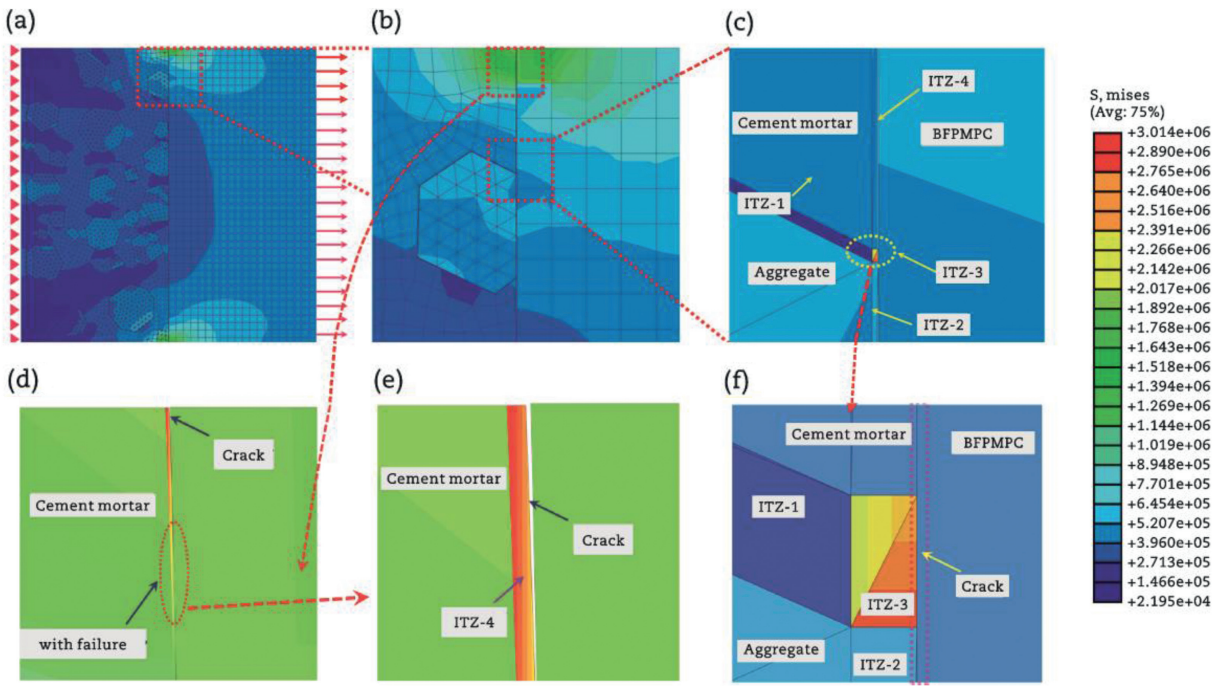

Fig. 12 – Failure of repair interface in a tensile state. (a) Mises nephogram of repair interface tensile damage. (b) Partial enlargement nephogram for interface tensile damage. (c) Mises nephogram of ITZ-3. (d) Damage fracture of repair interface edge position. (e) Detail of damage fracture for edge position of repair interface. (f) Enlarged view of damage fracture in the ITZ-3 region.

influence of tensile stress. It should be noted that there is concentrated stress with relatively large tensile stress in the ITZ-3 area.

With the repair interface beginning to be stressed, large stress appeared at the ITZ-3 near the end of the repair interface. The cracks develop from the end of the repair interface and ITZ-3 to the middle until fracture failure, as shown in Fig. 12(d)–(f), indicating that ITZ-3 with weak mechanical properties is more prone to fracture for its special location and structure. The nano-indentation experimental data of the ITZ showed that the elastic modulus of test points in ITZ-3 was smaller, which is the lowest mechanical property of various ITZ. It can be inferred that the ITZ-3 as a decisive factor has the worst mechanical properties among various ITZs in the repair interface, causing repair interface damage and fracture.

Additionally, it can be seen from Fig. 12(c) that the stress of ITZ-4 is affected by the upper surface of the repair interface and ITZ-3 with the stress distribution from the upper surface of the repair interface to ITZ-3 decreasing gradually at first and then increases suddenly. In a sense, the mechanical properties of the repair interface were also greatly affected by that of ITZ-4. Simultaneously, the smaller force of ITZ-1 and ITZ-2 may be affected by the difference in force position. The ITZ-1 is in cement concrete without being directly affected by the stress from BFPMPC, while ITZ-2 was not susceptible to damage for its favorable position in the repair interface structure.

4. Conclusions

This study investigated the repair interface of BFPMPC and concrete considering the ITZs between aggregate, ordinary Portland cement (OPC) mortar, and the ITZ between OPC mortar and aggregate. Nanoindentation tests and deconvolution analysis were conducted on the composite samples of 6 h and 3 d. The following conclusions can be drawn.

- The elastic modulus of the ITZ between cement mortar and aggregate with a width of around 20 μm can be regarded as 0.098 times of the aggregate and 0.51 times of the OPC mortar was investigated by the nanoindentation test.
- In the repair interface formed by BFPMPC and concrete at 6 h and 3 d, the elastic moduli of the ITZ with a width of about 10 μm of basalt fiber are 17.06 GPa and 30.21 GPa, respectively, which may be due to the low elastic modulus of the main matrix phase in the repair interface. In the BFPMPC paste, the elastic modulus of ITZ with a width of about 10–20 μm of basalt fiber is 62.01 GPa and 78.93 GPa, respectively.
- The ITZ-2 formed by BFPMPC and OPC mortar has roughly the same mechanical properties as the ITZ-4 between basalt aggregate and BFPMPC.
- Numerical simulation results of tensile fracture show that the crack develops from the end of the repair interface and ITZ-3 to the middle until fracture failure. But in the

shear fracture state, the crack developed from the upper end of the interface to the vicinity of the ITZ-3 area.

• The ITZ-3 formed by BFPMPC and the generated interface between OPC mortar and basalt aggregate has the worst mechanical properties among various ITZs in the repair interface, as a decisive factor for causing repair interface damage and fracture.

It is concluded that the mechanical properties of the repaired interface between the BFPMPC and old cement concrete as the initial exploration were studied and characterized through nanoindentation experiment and numerical simulation in this paper for the first time. The results not only obtained the elastic modulus data of ITZs, but also determined the numerical relationship of each ITZ, and analyzed the mechanical properties of the repaired interface. Unfortunately, due to the complexity of the bonds for the repaired interface, the defects in shear and tensile constitutive relations of interface interaction have not been thoroughly studied in this paper. Therefore, future work will focus on exploring the interface behavior between BFPMPC mortar and cement concrete and establishing a multi-scale interface model to study and characterize the action behavior of ITZ in detail. The finite element method (FEM), artificial neural network (ANN), and interface mechanics will be combined more effectively.

Conflict of interest

Changjun Zhou is a young academic editor of Journal of Traffic and Transportation Engineering (English Edition) and was not involved in the editorial review or the decision to publish this article. All authors declare that there are no competing interests.

Acknowledgments

This study is financially supported by the Fundamental Research Funds for the Central Universities (DUT20JC50, DUT17RC (3)006), the National Natural Science Foundation of China (51508137), and the Research Center of Civil Aviation Airport Safety and Operation Engineering Technology (KFKT2021-01). The authors appreciate the help from PhD candidate Fei Liu for conceptualization, methodology, writing-original draft, software, and data curation. Baofeng Pan, Ge Li, Xiaocun Wang, and Jiaquan Li contributed equally to this work.

REFERENCES

Acker, P., 2001. Micromechanical analysis of creep and shrinkage mechanisms. In: The Sixth International Conference of Creep, Shrinkage and Durability Mechanics of Concrete and Other Quasi-Brittle Materials, Cambridge, 2001.

Constantinides, G., 2002. The elastic properties of calcium leached cement pastes and motars: a multi-scale investigation. MIT CEE Report R02-01. Massachusetts Institute of Technology, Cambridge.

da Silva, W.R.L., Němečcek, J., Štemberk, P., 2014. Methodology for nanoindentation-assisted prediction of macroscale elastic properties of high performance cementitious composites. Cement and Concrete Composites 45, 57–68.

Das, S., Yang, P., Singh, S.S., et al., 2015. Effective properties of a fly ash geopolymer: synergistic application of X-ray synchrotron tomography, nanoindentation, and homogenization models. Cement and Concrete Research 78, 252–262.

Dong, Q., Zhao, X., Chen, X., et al., 2023. Numerical simulation of mesoscopic cracking of cement-treated base material based on random polygon aggregate model. Journal of Traffic and Transportation Engineering (English Edition) 10 (3), 454–468.

Feng, H., Li, Z., Wang, W., et al., 2021. Deflection hardening behaviour of ductile fibre reinforced magnesium phosphate cement-based composite. Cement and Concrete Composites 121, 104079.

Feng, P., Zhou, S., Zhao, J., 2016. Effect of cattle manure ash on workability and mechanical properties of magnesium phosphate cement. Construction and Building Materials 129, 79–88.

Gao, Y., Zhu, X., Corr, D.J., et al., 2019. Characterization of the interfacial transition zone of CNF-reinforced cementitious composites. Cement and Concrete Composites 99, 130–139.

Golewski, G.L., 2021. The beneficial effect of the addition of fly ash on reduction of the size of microcracks in the ITZ of concrete composites under dynamic loading. Energies (Basel) 14 (3), 668.

Karimzadeh, A., Koloor, S.S.R., Ayatollahi, M.R., et al., 2019. Assessment of nano-indentation method in mechanical characterization of heterogeneous nanocomposite materials using experimental and computational approaches. Scientific Reports 9 (1), 15763.

Kim, S.M., Abu Al-Rub, R.K., 2011. Meso-scale computational modeling of the plastic-damage response of cementitious composites. Cement and Concrete Research 41 (3), 339–358.

Königsberger, M., Hlobil, M., Delsaute, B., et al., 2018. Hydrate failure in ITZ governs concrete strength: a micro-to-macro validated engineering mechanics model. Cement and Concrete Research 103, 77–94.

Le Rouzic, M., Chaussadent, T., Stefan, L., et al., 2017. On the influence of Mg/P ratio on the properties and durability of magnesium potassium phosphate cement pastes. Cement and Concrete Research 96, 27–41.

Li, P., Ma, Z., Zhang, Z., et al., 2019. Effect of gypsum on hydration and hardening properties of alite modified calcium sulfoaluminate cement. Materials 12 (19), 3131.

Li, Y., Zhang, G., Wang, Z., et al., 2018. Experimental-computational approach to investigate compressive strength of magnesium phosphate cement with nanoindentation and finite element analysis. Construction and Building Materials 190, 414–426.

Liu, F., Pan, B., Cao, P., et al., 2021. Multi-scale characterization on behaviors of the interface between magnesium phosphate cement and portland cement. Construction and Building Materials 275, 122139.

Liu, Y., Jia, M., Song, C., et al., 2020. Enhancing ultra-early strength of sulphoaluminate cement-based materials by incorporating graphene oxide. Nanotechnology Reviews 9 (1), 17–27.

Liu, F., Pan, B., Zhou, C., 2022. Experimental study on a novel modified magnesium phosphate cement mortar used for rapid repair of portland cement concrete pavement in seasonally frozen areas. Journal of Materials in Civil Engineering 34 (3), 0004121.

Mondal, P., Shah, S.P., Marks, L., 2007. A reliable technique to determine the local mechanical properties at the nanoscale for cementitious materials. Cement and Concrete Research 37, 1440–1444.

Piasta, W., Góra, J., Budzyn, W., 2017. Stress-strain relationships and modulus of elasticity of rocks and of ordinary and high performance concretes. Construction and Building Materials 153, 728–739.
Qin, J., Qian, J., Dai, X., et al., 2021. Effect of water content on microstructure and properties of magnesium potassium phosphate cement pastes with different magnesia-to-phosphate ratios. Journal of the American Ceramic Society 104 (6), 2799–2819.
Qin, J., Qian, J., Li, Z., et al., 2018a. Mechanical properties of basalt fiber reinforced magnesium phosphate cement composites. Construction and Building Materials 188, 946–955.
Qin, J., Qian, J., You, C., et al., 2018b. Bond behavior and interfacial micro-characteristics of magnesium phosphate cement onto old concrete substrate. Construction and Building Materials 167, 166–176.
Sorelli, L., Constantinides, G., Ulm, F., et al., 2008. The nano-mechanical signature of ultra high performance concrete by statistical nanoindentation techniques. Cement and Concrete Research 38 (12), 1447–1456.
Sun, X., Gao, Z., Cao, P., et al., 2019. Mechanical properties tests and multiscale numerical simulations for basalt fiber reinforced concrete. Construction and Building Materials 202, 58–72.
Suwanmaneechot, P., Aili, A., Maruyama, I., 2020. Creep behavior of C-S-H under different drying relative humidities: interpretation of microindentation tests and sorption measurements by multi-scale analysis. Cement and Concrete Research 132, 106036.
Tan, Y., Yu, H., Sun, S., et al., 2020. Properties and microstructure of basic magnesium sulfate cement: influence of silica fume. Construction and Building Materials 266, 121076.
Wang, N., Yu, H., Bi, W., et al., 2018. Effects of sodium citrate and citric acid on the properties of magnesium oxysulfate cement. Construction and Building Materials 169, 697–704.
Wu, C., Yu, H., Zhang, H., et al., 2015. Effects of phosphoric acid and phosphates on magnesium oxysulfate cement. Materials and Structures 48 (4), 907–917.
Xi, X., Yin, Z., Yang, S., et al., 2021. Using artificial neural network to predict the fracture properties of the interfacial transition zone of concrete at the meso-scale. Engineering Fracture Mechanics 242, 107488.
Xu, X., Hu, Z., Duan, L., et al., 2020. Investigation of high volume of CFBC ash on performance of basic magnesium sulfate cement. Journal of Environmental Management 256, 109878.
Yang, C., 2003. Effect of the interfacial transition zone on the transport and the elastic properties of mortar. Magazine of Concrete Research 55 (4), 305–312.
Yang, N., Shi, C., Yang, J., et al., 2014. Research progresses in magnesium phosphate cement-based materials. Journal of Materials in Civil Engineering 26 (10), 1–8.
Zeng, X., Yu, H., 2020. Research on technology of performance improvement of basic magnesium sulfate cement–BMS. Structural Concrete 24 (3), 4313–4321.
Zhang, F., Guo, H., Hu, D., et al., 2018. Characterization of the mechanical properties of a claystone by nano-indentation and homogenization. Acta Geotechnica 13 (6), 1395–1404.
Zheng, Y., Zhou, Y., Huang, X., et al., 2022. Effect of raw materials and proportion on mechanical properties of magnesium phosphate cement. Journal of Road Engineering 2 (3), 243–251.
Zhou, C., Chen, L., Zheng, S., et al., 2020. Rheological, mechanical, and abrasion characteristics of polymer-modified cement mortar and concrete. Canadian Journal of Civil Engineering 1237 (9), 1226–1237.
Zhu, X., Yuan, Y., Li, L., et al., 2017. Identification of interfacial transition zone in asphalt concrete based on nano-scale metrology techniques. Materials & Design 129, 91–102.

Fei Liu is studying for a doctor's degree in Dalian University of Technology, China. His current focus is on the application and promotion of rapid repair materials.

Baofeng Pan is a professor and doctoral supervisor in Faculty of Infrastructure Engineering, Dalian University of Technology. He was the former party branch secretary and vice president of the College of Traffic and Transportation. He is mainly engaged in the research and development of road materials. In recent years, he has hosted or participated in 40 National Natural Science Foundation of China; two provincial ministerial science and technology progress awards, one municipal science and technology progress award; published nearly 50 academic papers and 9 academic monographs, and authorized 3 invention patents.

Changjun Zhou serves as associate professor in Faculty of Infrastructure Engineering, Dalian University of Technology. He won his PhD degree in civil engineering from University of Tennessee, Knoxville. His research interests include long-life pavements, sustainable paving materials, paving material durability.

Ge Li is working in Tongren City Transportation Bureau, China. He mainly engaged in pavement construction and maintenance, etc.

Xiaocun Wang is a senior engineer and PhD in geotechnical engineering of Tongji University, a post-doctoral fellow in engineering mechanics at the University of Science and Technology Beijing, and a member of the China Foundation Treatment Academic Committee. As a professional person in charge, he has been engaged in preliminary consulting work and related design work such as pre-approval and feasibility studies for large-scale civil airports such as Kunming Changshui Airport, Qingdao New Airport, and Chengdu New Airport.

Jiaquan Li is studying for a master's degree in Dalian University of Technology, China. His current focus is on the application and promotion of road engineering and structural design theory.